Chemical Engineering Journal 530 (2026) 173755

Contents lists available at ScienceDirect

Chemical Engineering Journal

journal homepage: www.elsevier.com/locate/cej

Interplay of cross-reading, pressure and co-evaporation speed on triple-source FA-based perovskite films and devices

Reinder K. Boekhoff [a,b,*], Lara M. van der Poll [a,b], Jin Yan [a,b], Aidan le Roux [b], Daan Bakker [b], Judah Robson [b], Arno H.M. Smets [a], Tom J. Savenije [b], Luana Mazzarella [a,**]

[a] PVMD Group, Delft University of Technology, Mekelweg 4, 2628 CD, Delft, the Netherlands
[b] Department of ChemE, Delft University of Technology, Van der Maasweg 9, 2629 HZ, Delft, the Netherlands

ARTICLE INFO

Keywords:
Co-evaporation
Thermal evaporation
Cross-reading
Deposition speed
Perovskite
Perovskite solar cells

ABSTRACT

Hybrid organic-inorganic perovskites (PVKs) offer exceptional optoelectronic performance, yet reproducible and scalable co-evaporation remains challenging. This study examines the interplay of factors affecting compositional control during three-source PVK deposition. We identify chamber pressure, precursor cross-contamination, and flux instability – especially from organic salts such as formamidinium iodide (FAI) – as major sources of variability. A critical influence is the occurrence of *cross-reading*, where omnidirectional evaporation of FAI contributes to the reading on the quartz crystal microbalance (QCM) sensors monitoring the inorganic precursors like caesium bromide (CsBr) and lead iodide (PbI_2) even though shielding is present. This effect, strongly dependent on FAI load, deposition rate, and QCM sensor position, erroneously inflates measured fluxes, leading to inaccurate rate control and unintentional compositional drift. Maintaining A-, B- and X-site stoichiometry therefore requires dynamic adjustment of precursor rates, particularly at higher deposition speeds where mean free path limitations come into play. We demonstrate the successful deposition of perovskite layers at a deposition speed of 27.8 nm min^{-1} as the practical ceiling for the investigated $Cs_xFA_{1-x}Pb(I_{1-x}Br_x)_3$ composition within our experimental framework. These findings highlight the delicate balance between deposition speed, precursor stability, and film quality, underscoring the need for improved delivery systems - such as continuous precursor feedthrough, multiple organic sources, alternative vapor transport or flash evaporation methods – to achieve reproducible, fast and large-scale fabrication of high-performance PVK films.

1. Introduction

Over the last decade, perovskite solar cells (PSCs) have gained significant attention due to their ease of fabrication and unprecedented rapid increases in power conversion efficiencies [1]. A crucial step in the production of a PSC is the deposition of the perovskite absorber (PVK) layer. Traditionally, solvent-based methods are used to create the PVK layer, starting from a solution that contains the precursor materials [2,3]. This method suffers from disadvantages such as the use of often toxic solvents and a difficult to control crystallization of the layer due to variations in the solubility of the precursors [4]. Besides, growing conformal layer on fully textured silicon, which is necessary for tandem configurations, is not trivial [5–7].

An alternative route to fabricate PVK absorbers is through vacuum-based deposition methods, which was first introduced by Liu *et al.* in 2013 [8]. Vacuum-based deposition, specifically thermal evaporation (TE), enables the growth of highly uniform layers with nanometer-scale control [5–7]. The solid precursors are heated in a vacuum chamber until they sublimate and subsequently deposit onto a substrate. In addition, vacuum-based methods are well-established in the semiconductor industry which is favorable for future industrialization. However, significantly longer deposition times are required compared to solution-based methods.

The evaporation of the solid precursors can be carried out sequentially, alternating the evaporation of the individual precursor layers [9–11]. This approach has demonstrated more control over the deposition process, as the individual layer thicknesses can be tuned to ensure the formation of a stoichiometric layer [12,13]. In lab-scale set-ups these depositions take longer because of the separate heating and deposition steps for individual precursors. Besides, a post-deposition annealing step

* Correspondence to: R.K. Boekhoff, PVMD Group, Delft University of Technology, Mekelweg 4, 2628 CD, Delft, the Netherlands.
** Corresponding author.
E-mail addresses: R.K.Boekhoff@tudelft.nl (R.K. Boekhoff), L.Mazzarella@tudelft.nl (L. Mazzarella).

https://doi.org/10.1016/j.cej.2026.173755
Received 2 December 2025; Received in revised form 20 January 2026; Accepted 2 February 2026
Available online 3 February 2026

is necessary to mix the precursors and form the PVK. It has been reported that for PVK layers thicker than 400 nm multiple alternating precursor cycles could be necessary to ensure a homogeneous layer, which can further increase the required deposition time [11]. Alternatively, co-evaporation [8,14,15] consists of the simultaneous precursor deposition from two or more sources, enabling a single-step production of PVK layers. Compared to the sequential method, co-evaporation is faster and does not suffer from diffusion and mixing limitations of the precursor materials. Nevertheless, co-evaporation is inherently complex, and this complexity increases with the number of sources involved. The complicating factor is the limited control over the possible collisions and reactions of the simultaneously sublimated species, leading to a less stable and less reproducible process.

In the co-evaporation of PVK layers, most of the complexities arise from the evaporation behaviour of the formamidinium iodide (FAI) precursor. Unlike inorganic precursors such as lead iodide (PbI_2) and caesium bromide (CsBr), which exhibit directional evaporation behaviour under vacuum conditions, organic compounds like FAI and methylammonium iodide (MAI) exhibit significantly more omnidirectional evaporation behaviour [16], due to molecular dissociation and scattering, leading to an increase in chamber pressure [17].

To make fully thermally evaporated PVKs commercially viable, a deeper understanding of the reproducibility and high-speed processability of the evaporated PVK layers is essential. Addressing these challenges will be necessary to determine the viability of co-evaporation as a competitive route for large-scale PSC production. Until then, as PSC technology moves closer to commercialization, it remains uncertain which manufacturing method – solution-based, vapor-based or hybrid [5] - will prove most cost-effective and reliable for large-scale module production.

Abzieher *et al.* demonstrated that, for vapor-deposited PVK layers to become commercially attractive, deposition speeds must reach approximately 1000 nm min^{-1} [18], enabling the full absorber to be deposited within 1 min. Works by Dewi *et al.* and Piot *et al.* have shown that the laboratory-scale fast dual-source co-evaporation of $MAPbI_3$ at 20 nm min^{-1} is feasible without significant losses in device performance [19,20]. Recently, Feeney *et al.* reported that increasing deposition rates to 27 nm min^{-1} leads to a performance drop due to spit defects caused by degraded FAI material in the PVK layer, which act as recombination centers [21].

Current approaches for TE of organic precursor salts still fall short of achieving the control required for industrial relevance. In this work, we investigate the processing challenges that arise when increasing the deposition rate of lab-scale co-evaporated $Cs_xFA_{1-x}Pb(I_{1-x}Br_x)_3$ layers up to 27.8 nm min^{-1}. We first deposit PVK layers using identical recipe settings and assessed their reproducibility by analysing preferential orientation through XRD. Examination of the process development across different batches reveals variations in chamber pressure. We then investigated deeper how pressure influences the deposition process, PVK growth and film composition. Afterwards, we investigate how increasing the deposition speed further affects the chamber pressure and what additional processing challenges arise when scaling up deposition speeds. We find that especially FAI-induced pressure fluctuations – resulting in cross-reading and unstable precursor fluxes – significantly influence the process outcomes. In our understanding cross-reading between the organic precursor source and the other QCM sensors persists even with shielding, and becomes particularly pronounced at higher deposition speeds.

2. Results and discussion

2.1. Reproducibility

We investigated the co-evaporation of PbI_2, CsBr and FAI precursors to obtain $Cs_xFA_{1-x}Pb(I_{1-x}Br_x)_3$ PVK layers with a thickness of approximately 700 nm. Fig. 1a shows a simplified schematic of our deposition chamber which includes 4 sources. The three heated precursor sources used in the depositions discussed in this paper are depicted in orange and shown in their relative positions. Also depicted are the corresponding QCMs and the sublimation cones projecting the sublimated precursors towards the rotating target substrate. The PVK layers are processed as described in the experimental section in the SI. Fig. 1b shows the normalized X-ray diffraction (XRD) patterns of four co-evaporated PVK layers all deposited using the same deposition rate parameters (CsBr at 0.2 Å s^{-1}, PbI_2 at 1.7 Å s^{-1} and FAI at 1.9 Å s^{-1}, see Table S1). The diffraction patterns exhibit several peaks corresponding to the (100), (110), (111), (200), (210), (220) and (300) crystallographic planes, characteristic of the photoactive cubic PVK phase. By analysing the XRD patterns a preferential orientation of the PVK layers can be distinguished, which tells us something about the reproducibility of the process. The same process repeated twice, should result in a similar layer with similar preferential ordering. Interestingly, despite following the same deposition recipe including deposition rates (see Fig. S1), the resulting XRD patterns—particularly the relative peak intensities—differ significantly among the different batches. For batch 1 and 4, the peak position and intensity seem to mostly align with predominant peaks corresponding to the (100) and (200) planes. A slightly larger (100)/(210) intensity ratio is observed in batch 1 compared to batch 4. Batch 3 deviates notably from the other samples, displaying the presence of a PbI_2 (100) diffraction peak ($2\theta = 12.7°$), along with less intense (100) and (200) PVK peaks and an intense (210) diffraction peak. Batch 2 also exhibits a preferred orientation along the (210) plane, but without the PbI_2 peak observed in batch 3. To study the reproducibility of the resulting layers in terms of opto-electronic and optical properties we look at the Time-Resolved Microwave Conductivity (TRMC) and Transmission results for the four different batches. The

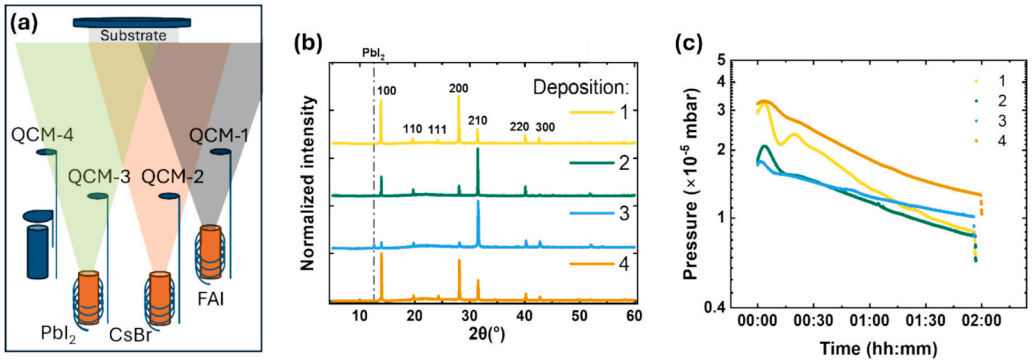

Fig. 1. (a) Schematic illustration of the TE chamber used for the co-evaporation of PVK layers and (b) XRD patterns of PVK layers deposited through TE utilizing identical process recipe settings after annealing treatment on a hotplate at 150 °C for 10 min. (c) Pressure evolution in the evaporation chamber during depositions 1–4.

intensity normalised photoconductance traces are visible in Fig. S2. TRMC enables the investigation of charge carrier recombination pathways and mobility-yield products, as described by Hutter *et al.* [22]. The TRMC signal decays for batch 1 and 4 are nearly identical and indicate a dominant second-order recombination mechanism in both PVK layers. However, the mobility-yield product is significantly higher for batch 4 compared to batch 1. Batch 2 exhibits a significantly shorter charge carrier lifetime and reduced peak signal height in the TRMC response, however, second order recombination still seems to be the most dominant recombination pathway. From the transmission spectra in Fig. S3a, we can see that the absorption onset varies between the batches, indicating a different composition. We see that batch 2 has a significantly larger transmission than the other batches. We relate this to incomplete conversion of the PVK precursors into photoactive PVK. We tried annealing at 170 °C instead of the regular 150 °C, which indeed decreased the transmission (Fig. S3a), but only slightly increased the preferential orientation along the (210) plane (Fig. S3b).

We can conclude from Fig. 1b, Fig. S2 and Fig. S3a that despite the process control settings being identical for the four layers, the resulting layers are different, both in their crystal orientation, but also optically as indicated by the transmission spectra in Fig. S3a. This observation highlights one of the main challenges faced when co-evaporating $Cs_xFA_{1-x}Pb(I_{1-x}Br_x)_3$ PVK layers, which is the poor reproducibility between batches.

By analysing the deposition conditions for the layers shown in Fig. 1b, we noticed that the pressure evolution in the evaporation chamber as a function of time differs substantially for the four batches as seen in Fig. 1c. In the next section we evaluate the effect of the pressure on the co-evaporation process.

2.2. Influence of FAI on pressure, precursor flux and PVK composition

To confirm the evaporation of FAI has the strongest influence on the chamber pressure, we first heated the two inorganic sources simultaneously, followed by heating the FAI source. During the experiment, we monitored the evolution of the pressure and the source temperatures for all three precursors, as shown in Fig. 2a. The data reveals that heating the inorganic precursors (PbI_2 and CsBr) has minimal impact on the pressure, which remains stable at approximately $3{\cdot}10^{-7}$ mbar. The slight temporal increase of the pressure observed upon heating the inorganics may be ascribed to the sublimation of residual impurities. In contrast, heating the FAI crucible results in an almost immediate and continuous rise in pressure, reaching up to approximately $1{\cdot}10^{-5}$ mbar, confirming its dominant influence on the vacuum.

Literature reports that for deposition temperatures around 160 °C and above, FAI partially degrades and converts into a mix of formamidine, hydrogen iodide, hydrogen cyanide, 1,3,5-*sym*-triazine and ammonia[24]. Hence, the chamber pressure serves as an indication of the background concentration of FAI and its derivatives. In contrast, decomposition of CsBr and PbI_2 does not occur under co-evaporation conditions and therefore has a negligible effect on the pressure. To achieve reproducible FA-based co-evaporated PVK layers, the FAI source temperature must be kept as stable and as low as possible to ensure consistent vapor composition, reproducible FAI flux to the target substrate, and high material utilization efficiency (i.e. reduced losses due to scattering).

As the pressure is significantly influenced by the sublimation behaviour of FAI, maintaining a consistent pressure profile during each deposition is essential for reproducible PVK layer growth. In our system, direct pressure regulation is not available: thus, we opt to control the chamber pressure during co-evaporations by adjusting the amount of

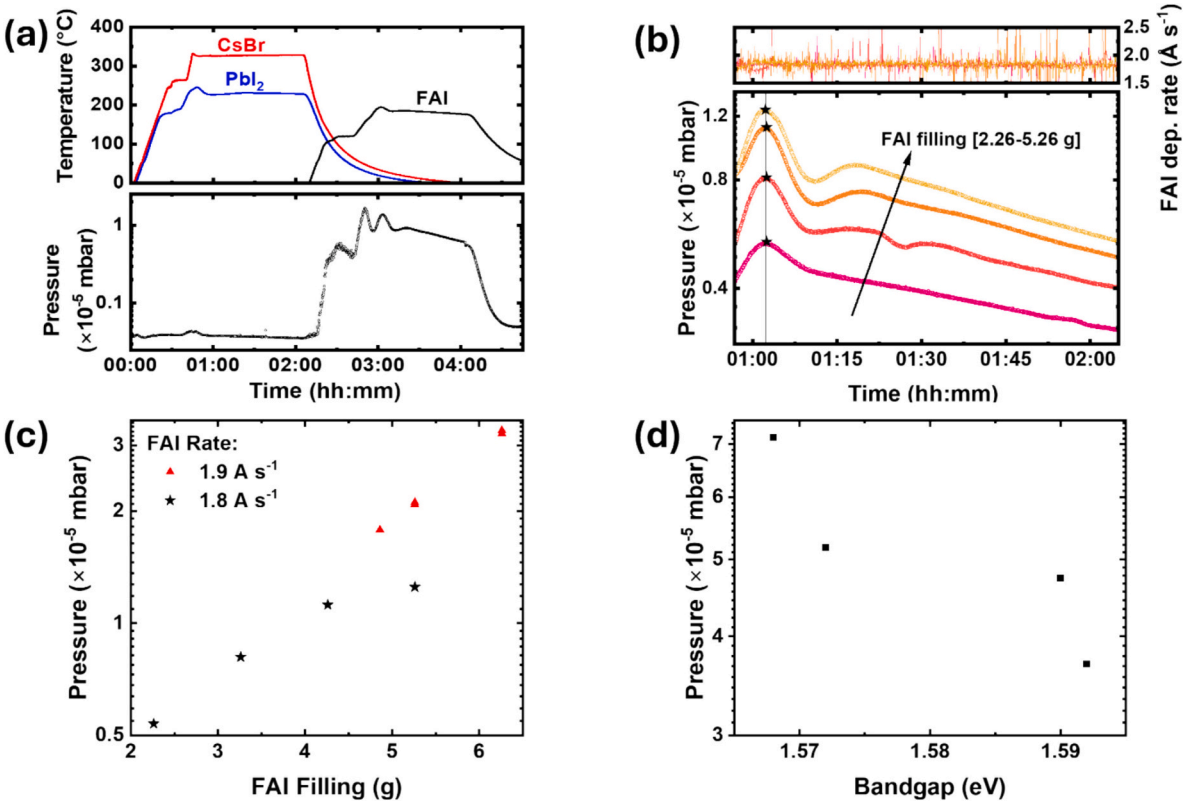

Fig. 2. Evolution of (a) source temperatures during deposition of CsBr (red), PbI2 (blue) and FAI (black) precursors (top) and the system's background pressure (bottom). (b) FAI deposition rate recorded over time (top) and the chamber pressure evolution for different FAI weights(bottom).Star symbols represent peak pressure values. (c) Peak pressure during FAI evaporation process as function of the FAI weight for two different deposition rates. The pressures corresponding to 1.8 Å s-1 are taken from panel b. (d) Peak pressure in the chamber as function of the resulting co-evaporated PVK bandgap.

FAI powder loaded into the crucible.

To illustrate the effect of FAI loading on the deposition, we recorded the pressure profiles during four subsequent FAI depositions, each performed at a constant deposition rate of 1.8 Å s^{-1}, while using different amounts of FAI powder in the crucible. The results are shown in Fig. 2b. To ensure consistency, fresh powder was used for each single deposition. Before ramping to the deposition temperature, an outgassing step at 120 °C for 10 min was included to remove volatile impurities from the FAI material. Despite the identical deposition rate as seen in the graph at the top of Fig. 2b, the pressure profiles exhibit noticeable variations depending on the initial crucible loading. When the FAI weight increased from 2.26 to 5.26 g, the chamber pressure nearly doubled. We extracted the peak chamber pressure observed immediately prior to the opening of the substrate shutter as a representative value for each run, indicated by the star symbols in Fig. 2b. Fig. 2c illustrates the relationship between peak chamber pressure and crucible filling at two different deposition rates. As expected, depositions conducted at higher rates–even with a difference in rate of only 0.1 Å s^{-1} – produce higher chamber pressures. In our system, the crucible is initially heated to a fixed temperature close to the expected target deposition rate. From this temperature, a PID controller finds the target rate. However, a larger FAI loading leads to elevated vapor pressure and can result in a higher deposition rate at the same temperature. This causes the system to temporarily overshoot the target rate even when extended stabilization times are applied. This rate stabilization issue becomes particularly critical at higher deposition rates, where the time and temperature required to stabilize the rate begins to overlap with the thermal decomposition window of the FAI material [23]. As a result, careful tuning of the deposition recipe is essential whenever any parameter - such as rate, crucible filling, or temperature - is adjusted.

To investigate whether the deposition pressure influences the PVK composition, we deposited four PVK layers using identical deposition rates but varying crucible fillings. The PVK bandgap as a function of the pressure is shown in Fig. 2d. The XRD patterns for the corresponding layers are presented in Fig. S4a, showing a decreasing (100)/(210) peak intensity ratio with pressure. Fig. S4b shows a shift of the (100) peak position towards lower angles indicating an increase in the lattice spacing and changing PVK composition. Despite identical processing rates, higher deposition pressures consistently produced layers with lower bandgaps (Fig. S4c and d shows the transmission spectra and Tauc plots). These trends suggests that increased pressure may lead to greater incorporation of FAI into the PVK, or alternatively, reduced incorporation of CsBr, leading to a decrease in the PVK bandgap. Thus, even though our system executes an automated deposition sequence based on a predefined recipe to ensure reproducibility, the crucible filling remains a critical variable that influences the final layer composition.

Another contributing factor to the irreproducibility is the unintentional FAI deposition that can occur on the substrate during the rate stabilization phase, prior to the opening of the substrate shutter. Since the FAI source significantly influences the chamber pressure, it is reasonable to expect that some material also reaches the substrate. In fact, in our experiments, we observed thin layers deposited on the substrates even when the FAI source was heated and the substrate shutter remained closed. Longer stabilization times will result in more FAI being deposited prematurely onto the substrate, potentially affecting the nucleation and early growth of the PVK layer. Several studies have reported substrate-dependent variations in co-evaporated PVK layers [24–26], highlighting the importance of tightly controlling this effect to ensure reproducibility.

2.3. Cross-reading

QCM rate control remains one of the most widely used methods to control hybrid organic-inorganic PVK co-evaporation deposition processes. The relative position of the sources, shutters, and rate sensors is commonly considered to ensure no cross-reading among different sources [27]. This statement is valid for inorganic sources, where no pressure increases are observed. However, when we see a pressure increase in the system, we cannot neglect the cross-readings. To further investigate the origin of poor reproducibility and bandgap variations that were discussed in Section 2.2, we decided to dive deeper into the effects of cross-reading on co-evaporation depositions.

The impact of chamber pressure on cross-reading can be visualized using the measured readings on the four separate QCMs (see schematic in Fig. 3a) during FAI deposition. The results of this experiment are reported in Fig. 3b for FAI material evaporated at a constant deposition rate of 1.8 Å s^{-1}, targeting a thickness of 10.000 Å as read by QCM-1, which is positioned directly above the FAI source. The same experiment was repeated with varying FAI crucible filling to assess the influence of higher pressure on the cross-reading. Despite only the FAI source being active, all other QCMs registered substantial FAI deposition, and the cross-reading intensity correlates to the initial amount of FAI in the crucible. QCM-2 exhibited the highest cross-reading. Notably, QCM-4 showed an increase in cross-reading, surpassing even QCM-3 at higher crucible fillings. This behaviour could be linked to differences in the shielding geometry of the QCMs. The cross-reading experiment demonstrates that FAI vapor distributes broadly within the chamber and contributes to non-negligible cross-reading even on sensors monitoring inactive sources. Consequently, during co-evaporation processes, such cross-reading can distort the rate measurements of other precursors, leading to inaccurate flux control and unintended compositional deviations. Even QCM sensors that are shielded and not directly in the periphery of the organic source can exhibit significant readings due to chamber pressure effects and molecular scattering, as also noted by Mahmoud *et al.* [28]

2.4. Increasing deposition speed

Building on our understanding of how FAI vapor affects QCM readings and rate control, we investigated the possibility of increasing the co-evaporation deposition speed from 6.1 nm min^{-1} to 27.8 nm min^{-1} for a single PVK layer containing 12.000 Å of PbI_2, as measured by the QCM. As the FAI QCM rate increases, both chamber pressure (Fig. 2c) and hence cross-reading effects (Fig. 3b) intensify, as demonstrated in Sections 2.2 and 2.3. Therefore, achieving the desired PVK composition and bandgap requires a continuous adjustment of the CsBr deposition rate when varying the deposition speed. Since FAI vapor contributes an unintended signal to the CsBr QCM-2, this leads to an overestimation of the actual CsBr flux. As a result, maintaining the same A- and X-site stoichiometry in the PVK layer (ABX_3) requires adjusting the nominal CsBr rate beyond what simple scaling would predict (i.e. beyond doubling all individual rates when depositing the same PVK twice as fast). This effect is clearly observed in our experiments and is visualized in Fig. 3c. For layers with similar bandgaps, the FA/Cs thickness ratio measured on the QCMs 1 and 2 at the end of each deposition decreases by a factor of two when the FAI QCM rate is increased from 1.9 Å s^{-1} to 4.2 Å s^{-1}. Focusing on two depositions that yield nearly identical bandgaps (star symbols at ~1.567 eV), the FAI QCM rate increased more than twofold (from 1.9 Å s^{-1} to 4.2 Å s^{-1}), while the required CsBr QCM rate had to be increased fourfold (from 0.2 Å s^{-1} to 0.8 Å s^{-1}). Meaning that we need, as measured by the QCM, twice as much CsBr in the layer compared to the slower rate deposition to achieve a similar composition. This confirms that cross-reading –-originating from omnidirectional FAI vapor –artificially inflates the QCM reading on the CsBr monitor, causing a mismatch between the intended and actual PVK compositions. Consequently, the exact FA/Cs ratio in the layer does not directly correspond to the rate ratio used in the deposition recipe. Since the bandgaps of these layers remain nearly constant, the observed QCM FA/Cs discrepancy in Fig. 3c reflects a distortion in QCM readings, rather than a genuine compositional shift.

Tooling factors are typically determined for single-precursor layers and represent the ratio of material reaching the substrate relative to

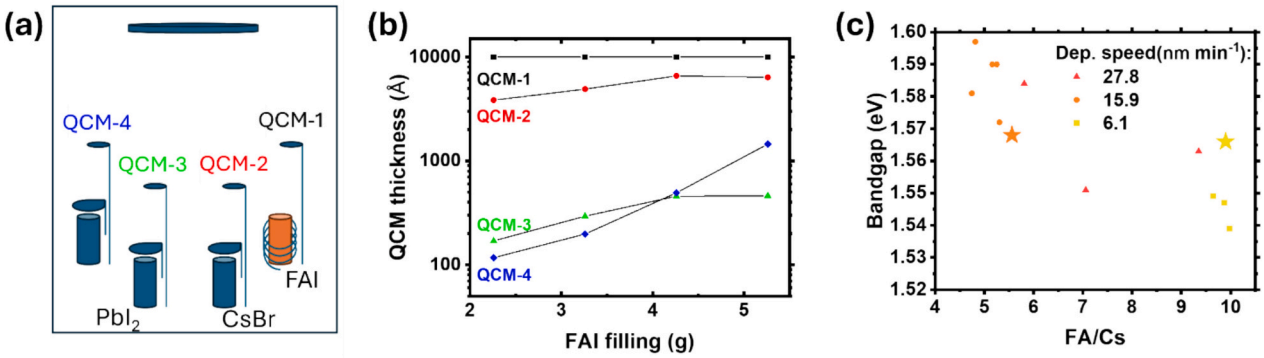

Fig. 3. (a) Schematic illustration of cross-reading test set-up (left) (b) cross reading on all four QCMs as measured when 10.000 Å of FAI was deposited on QCM-1. (c) Overview of bandgaps of co-evaporated PVKs versus the corresponding FA/Cs thickness ratio as measured on QCM-1 and QCM-2.

what is measured by the QCM. However, as demonstrated by the experiment carried out and shown in Fig. 3b, in co-evaporation processes, these tooling factors no longer hold because the actual tooling factor value is affected by the FAI reading on the inorganic QCMs.

Even though increasing the deposition speed presents challenges, we successfully produced solar cell devices which incorporated PVK layers deposited at different rates. Showing that it is possible to deposit $Cs_xFA_{1-x}Pb(I_{1-x}Br_x)_3$ at different deposition speeds. The solar cell parameter boxplots for the power conversion efficiency (PCE), fill factor (*FF*), short-circuit current density (J_{sc}) and open-circuit voltage (V_{oc}) are presented in Fig. 4. The *J-V* curves and solar cell parameters of the cells with the highest PCE for each deposition speed can be found in Fig. S6 and table S2 in the SI, respectively.

The deposition parameters and PVK layer thicknesses for these layers are summarized in Table S3. We find that the final PVK thickness slightly decreases when increasing the deposition speed, even though the QCM deposition limit for PbI_2 remained fixed at 12.000 Å again hinting at a slight overestimation of the PbI_2 flux, although less significant, as indicated by the minor cross-reading seen on QCM-3 in Fig. 3b.

Fig. 5a shows the XRD patterns of the resulting PVK layers that were incorporated in the PSCs. Significant PVK crystal growth is evident in the XRD pattern for all deposition speeds up to 27.8 nm min^{-1}. As shown in Fig. 5a, the highest deposition rate successfully demonstrated for deposition of co-evaporated $Cs_xFA_{1-x}Pb(I_{1-x}Br_x)_3$ layers from three sources was 27.8 nm min^{-1} for a 695 nm thick layer. Transmission spectra, Tauc plots, and SEM characterizations of these PVK layers are provided in the SI (Fig. S7, Fig. S8 and Fig. S9, respectively). Which show sharp absorption onsets for the different layers and densely packed PVK crystal grains. Fig. S9 shows relatively large PVK grains up to 1 µm for the co-evaporated PVK layers, generally co-evaporated PVK show relatively small grains when compared to solution processed counterparts [24]. We attribute the large grains to the grain formation and agglomeration during the annealing step after the PVK deposition.

Attempts to increase the deposition speed further resulted in XRD patterns dominated by the PbI_2 diffraction peak at $2\theta = 12.7°$, with negligible PVK diffraction peaks presence (Fig. 5a and b).

We observed significant PbI_2 excess in our attempts to deposit the PVK in a total deposition time of 15 min (total deposition time of PVK deposition at 27.8 nm min^{-1} is 25 min). This is demonstrated by the XRD pattern shown in Fig. 5b. To compensate for the PbI_2 excess, we gradually increased the FAI rate from 16.8 Å s^{-1} to 22.5 Å s^{-1} to enhance FAI incorporation. However, XRD reveals the limitations of co-evaporation at such elevated speeds. When examining layers deposited within 15 min at increasing FAI rates, the characteristic PVK peak remains

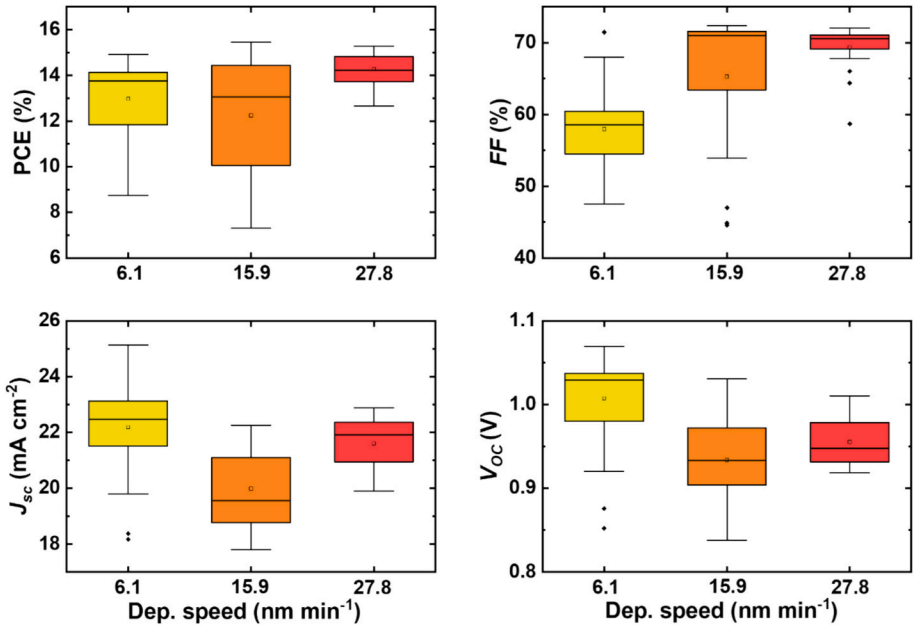

Fig. 4. Boxplots for PCE, FF, Jsc and Voc for the different batches of PSCs deposited at different deposition speeds.

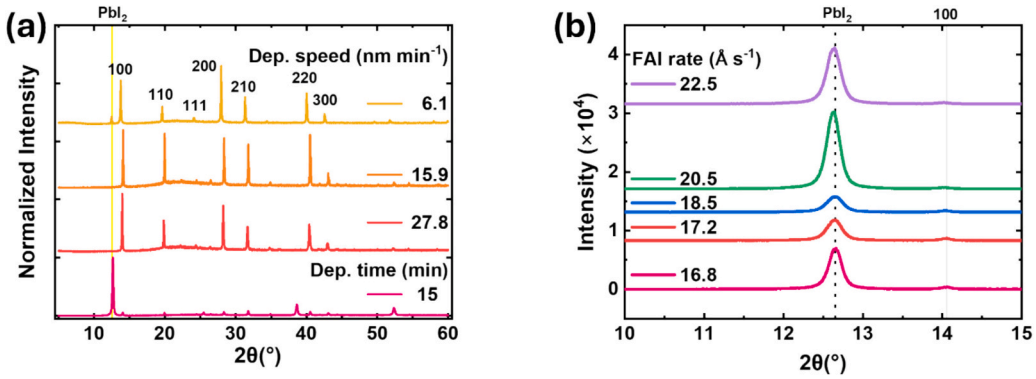

Fig. 5. (a) XRD patterns of PVK layers deposited at different total deposition times. (b) XRD patterns showing the PbI2 peak and the (100) PVK peak for 15 min depositions done with varying FAI rates.

suppressed. This behaviour is counterintuitive, as increasing FAI rate in a PbI_2-rich system would typically increase the PVK signal. This could be attributed to FAI decomposition and/or the reduced ability of FAI molecules to reach the substrate due to a shortened mean free path in the chamber at elevated pressures.

In our system, the source-to-substrate distance is fixed at approximately 35 cm. At the observed deposition pressures during the deposition taking 15 min, the estimated mean-free path (MFP) for FAI ranges between 25 and 35 cm as visualized in Fig. S10, which is shorter than the substrate distance. The derivation of the MFP calculation can be found in the SI. Interestingly, PbI_2, exhibits a slightly shorter MFP, however appears to be less affected. The pressure is related to the FAI precursor flux coming from the FAI source. We assume that the pressure right above the FAI source can be orders of magnitude higher than what is measured on the pressure sensor at the top of the evaporation chamber, which was previously also mentioned in the paper by Kroll *et al.* [23] Therefore, the mean-free path right above the source will be even lower than what is visualized in Fig. S9, causing more scattering and loss of flux to the

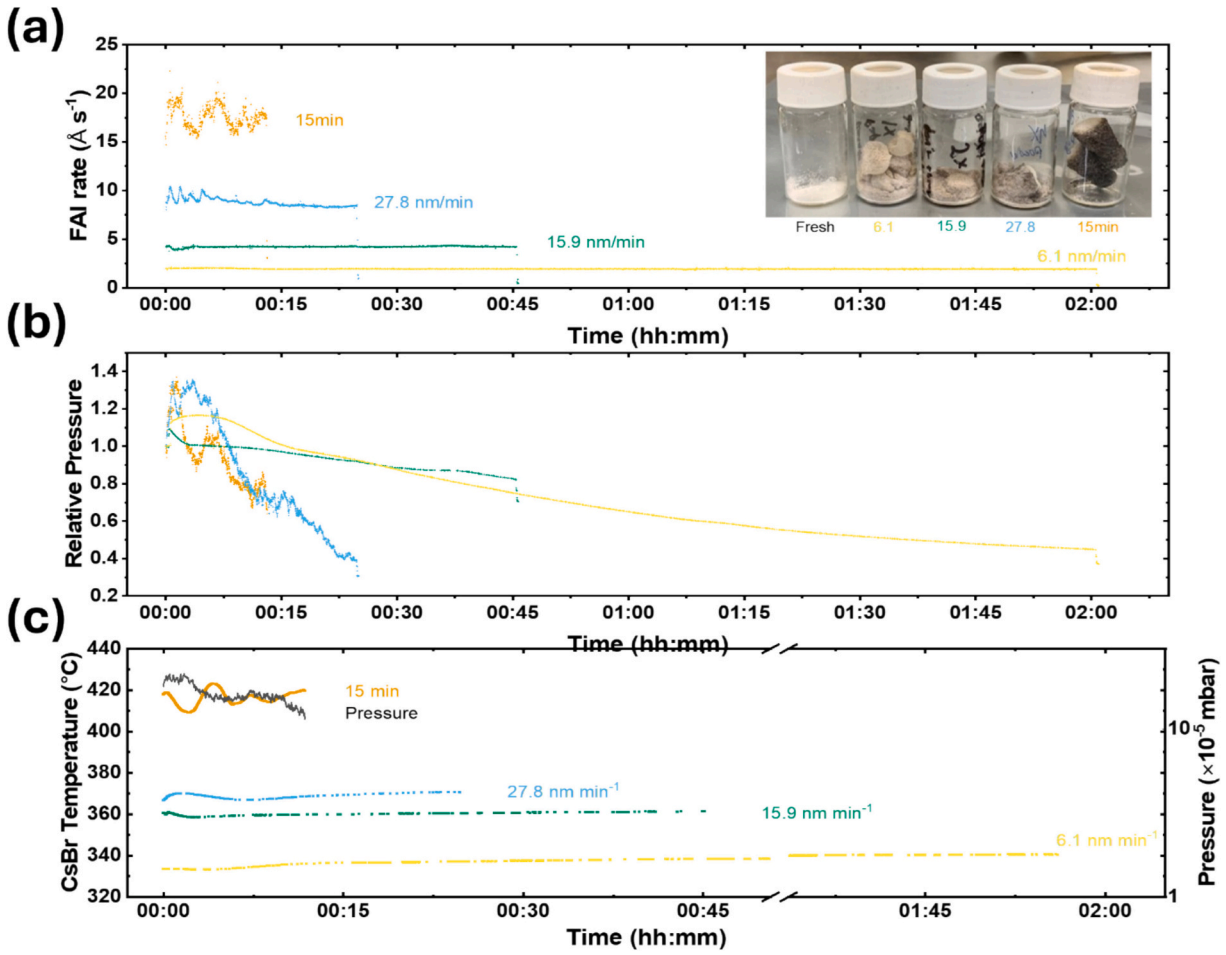

Fig. 6. (a) FAI rate and (b) normalized pressure evolution during co-evaporation depositions for different total deposition times. The inset shows a picture of the FAI after evaporations compared to the fresh powder. (c)CsBr temperature and system pressure evolution during co-evaporation deposition of a PVK layer over different deposition speeds.

substrate. This transport limitation likely contributes to the failure to form PVK at high FAI rates.

Once the MFP approaches the source-to-substrate distance, significant losses in precursor fluxes are expected. As a result, deposited layers become much thinner, and cross-reading on the other QCMs will increase substantially. This phenomenon likely explains the shift towards larger FA/Cs ratios observed at faster deposition speeds in Fig. 3c. During the deposition of the PVK at a rate of 27.8 nm min^{-1} the MFP drops to approximately 1 m. With respect to the slower depositions of 6.1 nm min^{-1} and 15.9 nm min^{-1}, where the MFP is in the range of three meters, the likelihood of FAI molecules reaching the substrate reduces.

To further elaborate on the increasing challenges associated with scaling up the co-evaporation processing speed, we examined the relationship between FAI deposition rate and the evolution of the pressure in the chamber. Fig. 6 presents four distinct scenarios encountered while co-evaporating PVK layers at different speeds.

As shown in Fig. 6a, the rate stability of the FAI precursor – as measured on QCM–1 decreases significantly with increasing deposition speed. For the 6.1 and 15.9 nm min^{-1} depositions, the FAI deposition rates remain relatively stable throughout the deposition. It is apparent that the 27.8 nm min^{-1} deposition exhibits a different behaviour: During the initial phase (0–6 min), the deposition rate fluctuates before stabilizing. In contrast to the other batches, the 15-min deposition shows extreme instability with the FAI rate fluctuating strongly around the target rate of 16.8 Å s^{-1} over the duration of the entire deposition. The corresponding relative pressure profiles, as seen in Fig. 6b, follow the FAI deposition rate over the course of the deposition. When these results are considered alongside the cross-reading data from Fig. 3b, we can assume that the rates measured on QCM-2 and QCM-3 – corresponding to the active CsBr and PbI_2 sources, respectively – are constantly changing due to varying unintended FAI contributions to the signal, due to the rapidly changing pressure over the deposition. This leads to instability in the apparent rate at the CsBr and PbI_2 sources, further complicating flux control and compositional accuracy during high-speed co-evaporation.

To further assess the impact of the deposition speed on the process stability, we plotted the CsBr source temperature during the deposition, as shown in Fig. 6c. For the 6.1, 15.9, and 27.8 nm min^{-1} depositions, the CsBr source temperature is stable throughout the deposition. Generally, the source temperature gradually increases over time to compensate for factors such as decreasing chamber pressure, reduced precursor powder weight, changes in the precursor surface area (e.g. powder clustering) and lower thermal contact with the crucible wall – all of which require higher crucible temperature to sustain the target flux. These observations explain the reasons why setting a fixed temperature for PbI_2 and CsBr sources does not results in a constant flux throughout the deposition. In contrast, the fastest deposition attempts in 15 min shows significant instability in the CsBr source temperature as it reacts to the pressure inside the chamber. When the pressure drops quickly after the start of the deposition, the CsBr source temperature increases to compensate for the loss of FAI cross-reading signal. This is followed by a slight overshoot of the target rate due to the PID settings of the crucible. Between 00:04 and 00:06 h, the deposition rate stabilizes briefly, but as the pressure continues to drop, the CsBr source temperature must increase further to maintain the desired rate. These fluctuations suggest that the system is approaching the limits of rate control under fast co-evaporation conditions. Since co-evaporation requires a constant flux of all precursors to the substrate, such instability poses a significant challenge to maintaining the layer‘s uniformity in stoichiometry.

2.5. Deposition rate limitation

In addition to the increasing difficulties with attaining stable deposition rates, another limiting factor emerges at elevated deposition rates: significant thermal degradation of FAI within the crucible during evaporation. Under typical co-evaporation conditions operating at lower rates, the temperature remains moderate enough to avoid significant decomposition of FAI during the deposition. However, the higher temperatures required for faster deposition rates accelerate the decomposition of the FAI powder [23]. Which is another explanation why we see less FAI incorporation in Fig. 5b upon increasing rates.

This degradation is visually confirmed in the inset of Fig. 6a. For each deposition, fresh FAI powder was used and the remaining powder collected from the crucible stored under nitrogen until a post-deposition characterization is performed. At lower deposition speeds, the used powder remains white at the core with darkened edges - indicating only partial degradation. In contrast, at higher deposition rates, the powder turns uniformly black throughout the crucible after a single run, suggesting complete decomposition. Under these conditions, the system fails to form a functional PVK layer (see Fig. 5a and b). The visual differences seen in the inset of Fig. 6a suggest degradation most likely due to coke formation, as previously proposed by others [29].

To elucidate the visual degradation of the FAI powders after processing at different speeds, additional spectroscopic analysis was performed. The powders in the inset of Fig. 6a were analysed with Fourier-Transform Infrared (FTIR). Fig. S11a shows the spectral region between 1400 and 1650 cm^{-1}. All the powder residues, independently of the deposition speed, exhibit the formation of the characteristic triazine C═N quadrant stretch vibration at 1558 cm^{-1} [30]. Besides, the region exhibits emerging features consistent with *s*-triazine based polymerization products [30,31].

Fig. S11b shows the C═N stretch regime for all the data sets. The fresh powder shows only a single dip at 1735 cm^{-1} corresponding to the C═N bond present in the formamidinium molecule. The powder residues after deposition at different speeds all exhibit peak splitting, indicating there is no longer a single uniform chemical species, but likely the presence of dimers and oligomers with slightly different bond strengths which causes the peak to split.

Furthermore, a stable and consistent flux is essential for achieving homogeneous mixing of precursors at the substrate during co-evaporation. However, rate stabilization is not instantaneous: both the crucible and the precursor material require time to reach thermal equilibrium. Because heating in vacuum occurs through the crucible walls, and the powder inside is not immediately at a uniform temperature, stabilization time is particularly critical for organic precursors like FAI.

To further elucidate the implication of our observations, we consider the nature of the organic salt. A salt in its solid phase is held together by electrostatic forces. Generally, the lattice energy for a salt is very large. For FAI, which contains the bulky organic FA^+ ion and the large I^- halide ion, the lattice energy is relatively small, hence it sublimates at low temperatures (< 200 °C) compared to other salts. The positive charge of the FA^+ ion is highly unfavourable in vacuum as it cannot be screened by its surroundings. This characteristic promotes the sublimation of neutral organic degradation products. The decomposition of FAI increases the number of vapor-phase molecules near the source, causing enhanced collisions and scattering throughout the evaporation chamber [24]. This results in a pressure increase in the reaction chamber upon heating of the FAI crucible, as shown in Fig. 2a. We would argue that co-evaporation from an initial FAI reservoir for extended periods is only possible if lattice energy is significantly lower than binding energy within the FA ion, as otherwise degradation would change the flux composition significantly over time. The paper by Kroll *et al.* [23] shows that evaporation of degradation products happens before 120 °C and that therefore co-evaporation from an initial reservoir is not a viable option.

These findings raise the question of whether high-speed hybrid organic-inorganic co-evaporation is viable at an industrial scale. While we reached a deposition speed of 27.8 nm min^{-1} in our fastest three-sources deposition, the precursor material was significantly degraded after a single deposition. One solution is to increase the number of co-

evaporation zones in a linear system, such as described in the study by Petry *et al.* [29], which could enable higher deposition speeds. Increasing the crucible-precursor contact area will lead to higher rates at the same temperature. However, this approach is only feasible for extended periods if the deposition temperature can be reduced below the degradation temperature.

For fully thermally evaporated hybrid organic-inorganic PVKs to be scalable, future research should be directed at maintaining a stable, high-quality precursor flux over an extended period of time. This could be achieved by using a continuous feedthrough of fresh precursor material into the source to prevent degradation prior to sublimation. Alternatively, different deposition methods for the organic precursor –such as vapor transport depositions, close-space sublimation [32] or flash-evaporation [33] –should be explored further.

3. Conclusion

This study highlights the complex interplay of factors that challenge the reproducibility and scalability of hybrid organic–inorganic PVK co-evaporation. Our results demonstrate that chamber pressure, precursor cross-contamination, and flux instability—particularly from organic sources like FAI—can significantly distort composition control and bandgap uniformity. A key finding is the presence of cross-reading, where omnidirectional FAI vapor unintentionally contributes readings to QCM sensors monitoring other precursors such as CsBr and PbI_2. This effect is strongly dependent on the amount of FAI powder in the crucible, the deposition rate, and the location of the sensors within the chamber. As a result, rate measurements are artificially inflated, leading to inaccurate flux control and compositional drift.

Achieving consistent A-, B- and X-site stoichiometry thus requires dynamic adjustment of precursor rates, especially under varying deposition speeds, where mean free path limitations lead to material losses and cross-reading causes unintentional compositional drift. These findings underscore that while faster co-evaporation offers potential for industrial throughput, the degradation of precursor material and difficulty in maintaining stable fluxes pose serious constraints. For the specific PVK composition investigated –based on three-sources co-evaporation– we successfully demonstrated 27.8 nm min^{-1} as the fastest deposition speed at which we were able to achieve high-quality PVK layers both on material and device-level.

Future research should therefore prioritize the development of strategies to stabilize precursor delivery—such as continuous feed-through systems, multiple organic sources, or alternative organic deposition techniques like vapor transport or flash-evaporation—to enable reliable large-scale fabrication of high-quality PVK layers.

CRediT authorship contribution statement

Reinder K. Boekhoff: Writing – review & editing, Writing – original draft, Visualization, Methodology, Investigation, Formal analysis, Data curation, Conceptualization. **Lara M. van der Poll:** Writing – review & editing, Conceptualization. **Jin Yan:** Writing – review & editing, Conceptualization. **Aidan le Roux:** Investigation. **Daan Bakker:** Investigation. **Judah Robson:** Investigation. **Arno H.M. Smets:** Writing – review & editing, Supervision, Project administration, Conceptualization. **Tom J. Savenije:** Writing – review & editing, Supervision, Project administration, Conceptualization. **Luana Mazzarella:** Writing – review & editing, Writing – original draft, Visualization, Supervision, Methodology, Formal analysis, Conceptualization.

Declaration of competing interest

The authors declare that they have no known competing financial interests or personal relationships that could have appeared to influence the work reported in this paper.

Acknowledgements

The authors thank Martijn Tijssen (PVMD group, Delft University of Technology, 2628 CD Delft, The Netherlands) and Bernardus Zijlstra (PVMD group, Delft University of Technology, 2628 CD Delft, The Netherlands) for support with TU Delft perovskite line. The authors thank Xiaohui Liu and Lars J. Bannenberg (Department of ChemE, Delft University of Technology, 2629 HZ Delft, The Netherlands) for support with XRD measurements. The authors thank Bahiya Ibrahim (Department of ChemE, Delft University of Technology, 2629 HZ Delft, The Netherlands) for support with transmission measurements.

Appendix A. Supplementary data

Supplementary data to this article can be found online at https://doi.org/10.1016/j.cej.2026.173755.

Data availability

Data will be made available on request.

References

[1] National Renewable Energy Laboratory, NREL, Best Research-Cell Efficiencies Chart, 2025 https://www.nrel.gov/pv/cell-efficiency (accessed November 3, 2025).
[2] A. Kojima, K. Teshima, Y. Shirai, T. Miyasaka, Organometal halide perovskites as visible-light sensitizers for photovoltaic cells, J. Am. Chem. Soc. 131 (2009) 6050–6051, https://doi.org/10.1021/ja809598r.
[3] R.A. Afre, D. Pugliese, Perovskite solar cells: a review of the latest advances in materials, fabrication techniques, and stability enhancement strategies, Micromachines (Basel). 15 (2024), https://doi.org/10.3390/mi15020192.
[4] A.A. Petrov, A.A. Ordinartsev, S.A. Fateev, E.A. Goodilin, A.B. Tarasov, Solubility of hybrid halide perovskites in dmf and dmso, Molecules 26 (2021), https://doi.org/10.3390/molecules26247541.
[5] F. Sahli, J. Werner, B.A. Kamino, M. Bräuninger, R. Monnard, B. Paviet-Salomon, L. Barraud, L. Ding, J.J. Diaz Leon, D. Sacchetto, G. Cattaneo, M. Despeisse, M. Boccard, S. Nicolay, Q. Jeangros, B. Niesen, C. Ballif, Fully textured monolithic perovskite/silicon tandem solar cells with 25.2% power conversion efficiency, Nat. Mater. 17 (2018) 820–826, https://doi.org/10.1038/s41563-018-0115-4.
[6] X. Luo, H. Luo, H. Li, R. Xia, X. Zheng, Z. Huang, Z. Liu, H. Gao, X. Zhang, S. Li, Z. Feng, Y. Chen, H. Tan, Efficient perovskite/silicon tandem solar cells on industrially compatible textured silicon, Adv. Mater. 35 (2023), https://doi.org/10.1002/adma.202207883.
[7] M. Roß, S. Severin, M.B. Stutz, P. Wagner, H. Köbler, M. Favin-Lévêque, A. Al-Ashouri, P. Korb, P. Tockhorn, A. Abate, B. Stannowski, B. Rech, S. Albrecht, Co-evaporated formamidinium lead iodide based perovskites with 1000 h constant stability for fully textured monolithic perovskite/silicon tandem solar cells, Adv. Energy Mater. 11 (2021), https://doi.org/10.1002/aenm.202101460.
[8] M. Liu, M.B. Johnston, H.J. Snaith, Efficient planar heterojunction perovskite solar cells by vapour deposition, Nature 501 (2013) 395–398, https://doi.org/10.1038/nature12509.
[9] D. Yang, Z. Yang, W. Qin, Y. Zhang, S. Liu, C. Li, Alternating precursor layer deposition for highly stable perovskite films towards efficient solar cells using vacuum deposition, J. Mater. Chem. A Mater. 3 (2015) 9401–9405, https://doi.org/10.1039/c5ta01824b.
[10] H. Hu, D. Wang, Y. Zhou, J. Zhang, S. Lv, S. Pang, X. Chen, Z. Liu, N.P. Padture, G. Cui, Vapour-based processing of hole-conductor-free CH3NH 3PbI3 perovskite/C60 fullerene planar solar cells, RSC Adv. 4 (2014) 28964–28967, https://doi.org/10.1039/c4ra03820g.
[11] J. Yan, J. Zhao, H. Wang, M. Kerklaan, L.J. Bannenberg, B. Ibrahim, T.J. Savenije, L. Mazzarella, O. Isabella, Crystallization process for high-quality Cs0.15FA0.85PbI2.85Br0.15 film deposited via simplified sequential vacuum evaporation, ACS Appl. Energy Mater. 6 (2023) 10265–10273, https://doi.org/10.1021/acsaem.3c00203.
[12] J. Yan, J. Nespoli, R.K. Boekhoff, H. Wang, T. Gort, M. Tijssen, B. Zijlstra, A. Houtepen, T.J. Savenije, O. Isabella, L. Mazzarella, Chloride-improved crystallization in sequentially vacuum-deposited perovskites for p-i-n perovskite solar cells, Sustain. Energy Fuels 9 (2025) 2729–2737, https://doi.org/10.1039/d4se01744g.
[13] J. Yan, L.S. Stickel, L. van den Hengel, H. Wang, P.R. Anusuyadevi, A. Kooijman, X. Liu, B. Ibrahim, A. Mol, P. Taheri, L. Mazzarella, O. Isabella, T.J. Savenije, Vacuum deposited perovskites with a controllable crystal orientation, J. Phys. Chem. Lett. 14 (2023) 8787–8795, https://doi.org/10.1021/acs.jpclett.3c01920.
[14] M. Roß, L. Gil-Escrig, A. Al-Ashouri, P. Tockhorn, M. Jošt, B. Rech, S. Albrecht, Co-evaporated p-i-n perovskite solar cells beyond 20% efficiency: impact of substrate temperature and hole-transport layer, ACS Appl. Mater. Interfaces 12 (2020) 39261–39272, https://doi.org/10.1021/acsami.0c10898.

[15] Y.H. Chiang, M. Anaya, S.D. Stranks, Multisource vacuum deposition of methylammonium-free perovskite solar cells, ACS Energy Lett. 5 (2020) 2498–2504, https://doi.org/10.1021/acsenergylett.0c00839.
[16] B.S. Kim, L. Gil-Escrig, M. Sessolo, H.J. Bolink, Deposition kinetics and compositional control of vacuum-processed CH3NH3PbI3Perovskite, J. Phys. Chem. Lett. 11 (2020) 6852–6859, https://doi.org/10.1021/acs.jpclett.0c01995.
[17] K.L. Heinze, O. Dolynchuk, T. Burwig, J. Vaghani, R. Scheer, P. Pistor, Importance of methylammonium iodide partial pressure and evaporation onset for the growth of co-evaporated methylammonium lead iodide absorbers, Sci. Rep. 11 (2021), https://doi.org/10.1038/s41598-021-94689-1.
[18] T. Abzieher, D.T. Moore, M. Roß, S. Albrecht, J. Silvia, H. Tan, Q. Jeangros, C. Ballif, M.T. Hoerantner, B.S. Kim, H.J. Bolink, P. Pistor, J.C. Goldschmidt, Y. H. Chiang, S.D. Stranks, J. Borchert, M.D. McGehee, M. Morales-Masis, J.B. Patel, A. Bruno, U.W. Paetzold, Vapor phase deposition of perovskite photovoltaics: short track to commercialization? Energy Environ. Sci. 17 (2024) 1645–1663, https://doi.org/10.1039/d3ee03273f.
[19] M. Piot, J.E.S. Alonso, K.P.S. Zanoni, N. Rodkey, F. Ventosinos, C. Roldán-Carmona, M. Sessolo, H. Bolink, Fast coevaporation of 1 μm thick perovskite solar cells, ACS Energy Lett. 8 (2023) 4711–4713, https://doi.org/10.1021/acsenergylett.3c01724.
[20] H.A. Dewi, E. Erdenebileg, D. De Luca, S.G. Mhaisalkar, A. Bruno, Accelerated MAPbI3 co-evaporation: productivity gains without compromising performance, ACS Energy Lett. 9 (2024) 4319–4322, https://doi.org/10.1021/acsenergylett.4c01597.
[21] T. Feeney, A. Miaskiewicz, J. Petry, F. Laufer, R. Singh, S. Severin, V. Škorjanc, A. Diercks, S. Maniyarasu, L. Korte, S. Albrecht, U.W. Paetzold, M. Roß, P. Fassl, High-rate FA-based co-evaporated perovskites: understanding rate limitations and practical considerations to overcome their impact, Adv. Funct. Mater. (2025), https://doi.org/10.1002/adfm.202517873.
[22] T.J. Savenije, D. Guo, V.M. Caselli, E.M. Hutter, Quantifying charge-carrier Mobilities and recombination rates in metal halide perovskites from time-resolved microwave photoconductivity measurements, Adv. Energy Mater. 10 (2020), https://doi.org/10.1002/aenm.201903788.
[23] M. Kroll, S.D. Öz, Z. Zhang, R. Ji, T. Schramm, T. Antrack, Y. Vaynzof, S. Olthof, K. Leo, Insights into the evaporation behaviour of FAI: material degradation and consequences for perovskite solar cells, sustain, Energy Fuel 6 (2022) 3230–3239, https://doi.org/10.1039/d2se00373b.
[24] T. Abzieher, T. Feeney, F. Schackmar, Y.J. Donie, I.M. Hossain, J.A. Schwenzer, T. Hellmann, T. Mayer, M. Powalla, U.W. Paetzold, From groundwork to efficient solar cells: on the importance of the substrate material in co-evaporated perovskite solar cells, Adv. Funct. Mater. 31 (2021), https://doi.org/10.1002/adfm.202104482.
[25] Z. Wang, M. Lyu, B.W. Zhang, M. Xiao, C. Zhang, E.Q. Han, L. Wang, Thermally evaporated metal halide perovskites and their analogues: film fabrication, applications and beyond, Small Methods 9 (2025), https://doi.org/10.1002/smtd.202301633.
[26] T. Feeney, J. Petry, A. Torche, D. Hauschild, B. Hacene, C. Wansorra, A. Diercks, M. Ernst, L. Weinhardt, C. Heske, G. Gryn'ova, U.W. Paetzold, P. Fassl, Understanding and exploiting interfacial interactions between phosphonic acid functional groups and co-evaporated perovskites, Matter 7 (2024) 2066–2090, https://doi.org/10.1016/j.matt.2024.02.004.
[27] L. Gil-Escrig, J. Nespoli, F.D. Elhorst, F. Ventosinos, C. Roldán-Carmona, L.J. A. Koster, T.J. Savenije, M. Sessolo, H.J. Bolink, Tuning substrate temperature for enhanced vacuum-deposited wide-bandgap perovskite solar cells: insights from morphology, charge transport, and drift-diffusion simulations, EES Solar 1 (2025) 391–403, https://doi.org/10.1039/d5el00021a.
[28] M.A.A. Mahmoud, Y. Gupta, O. Fischer, J.B. Landgraf, M. Bivour, J. Borchert, Unveiling the complexity of co-evaporation of perovskite: why Co-evaporation might not be the optimal choice. †, J. Mater. Chem. A Mater. (2025) https://doi.org/10.1039/D5TA08316H.
[29] J. Petry, V. Škorjanc, A. Diercks, T. Feeney, A. Morsa, S.R. Kimmig, J. Baumann, F. Löffler, S. Auschill, J. Damm, D. Baumann, F. Laufer, J. Kurpiers, M. Müller, L. Korte, S. Albrecht, M. Roß, U.W. Paetzold, P. Fassl, Industrialization of perovskite solar cell fabrication: strategies to achieve high-throughput vapor deposition processes, EES Solar 1 (2025) 404–418, https://doi.org/10.1039/d5el00069f.
[30] P.M.C. Matias, A.C. Ana, S.C.C. Nunes, A.A.C. Canelas Pais, D. Murtinho, A.J. M. Valente, Assessing interactions between antibiotics and triazine porous organic polymeric sorbents by photophysics, Environ. Pollut. 363 (2024), https://doi.org/10.1016/j.envpol.2024.125197.
[31] X. Yuan, K. Luo, K. Zhang, J. He, Y. Zhao, D. Yu, Combinatorial vibration-mode assignment for the FTIR spectrum of crystalline melamine: a strategic approach toward theoretical IR vibrational calculations of triazine-based compounds, J. Phys. Chem. A 120 (2016) 7427–7433, https://doi.org/10.1021/acs.jpca.6b06015.
[32] N. Rodkey, I. Gomar-Fernández, F. Ventosinos, C. Roldan-Carmona, L.J.A. Koster, H.J. Bolink, Close-space sublimation as a scalable method for perovskite solar cells, ACS Energy Lett. 9 (2024) 927–933, https://doi.org/10.1021/acsenergylett.3c02794.
[33] N. Rodkey, B. Huisman, H.J. Bolink, Incremental feeding of perovskite powders: angstrom-precision growth for single-source solar cell fabrication, Adv. Eng. Mater. 26 (2024), https://doi.org/10.1002/adem.202400636.

Glossary

A-, B-, and X-site: The three distinct crystallographic positions within the perovskite (ABX_3) Crystal structure.
Thermal evaporation: A thin film deposition technique where solid precursors are heated in vacuum until the sublimate and the resulting vapour deposits onto a cooler substrate to form a thin film.
Co-evaporation: A thin film deposition technique where multiple precursor sources are simultaneously heated under vacuum and sublimed to deposit a compound with precise controlled thickness and stoichiometry.
Sequential evaporation: A thin film deposition technique where precursors are deposited one after the other.
Stoichiometry: The precise quantitative combination of A-, B- and X- atom ratios required to form a perfect crystal.
Cross-reading: A measurement error where the vapour flux from one source is measured on the quartz-crystal microbalances that is intended to monitor the vapour flux of another source.
Quartz-Crystal Microbalance (QCM): An instrument used in vacuum deposition processing to measure the mass of a material being deposited onto a sensor by monitoring the change in the sensors oscillation frequency.
Precursor: The raw chemical starting material that is evaporated and reacts to form the target thin-film.
Mean free path: The average distance a molecule can travel before it collides with another molecule. In vacuum deposition it is affected by the pressure.
Hybrid organic-inorganic: Refers to a perovskite target composition containing both organic and inorganic A-site cations.
Omnidirectional: Refers to the evaporation behaviour of FAI. The low mean free path of the FAI molecules causes the vapour flux to scatter in all directions instead of creating a focused directional flow towards the substrate surface.
Annealing: A post-deposition thermal processing step applied to the as-deposited layers to induce crystallization, which is often necessary to form the perovskite structure.
Power Conversion Efficiency (PCE): A metric used to evaluate solar cell performance. The percentage of incident energy that is converted into usable electrical energy by the cell.
Perovskite Absorber (PVK) layer: The active layer in a perovskite solar cell with an ABX_3 crystal structure. The layer that absorbs sunlight which generates electron-hole pairs.
Perovskite Solar Cells (PSCs): Solar cells which use PVK as the active layer in the device architecture.
Preferential Orientation: The alignment of the crystallographic planes within a deposited film. Where a majority of the planes are along a specific crystallographic axis. Typically measured using XRD.
Recombination centers: Defects or impurities that are present within the PVK layer that lead to the recombination of electron-hole pairs which reduces the PCE of the cell.
Spit defects: Defects often caused by poor precursor evaporation which appear as localized imperfections or pinholes in the final thin film.
Sublimate: The transition of a substance directly from the solid phase to the gas phase, bypassing the liquid phase.